Muography for a dense tide monitoring network

Hiroyuki Tanaka (ht@eri.u-tokyo.ac.jp)
University of Tokyo

Research Article

Keywords:

Posted Date: February 3rd, 2022

DOI: https://doi.org/10.21203/rs.3.rs-1304616/v1

Abstract

Sub-hourly to seasonal and interannual oceanographic phenomena can be better understood with high special resolution and high frequency tidal observations. However, while current tidal measurements can provide sufficiently high observational density in the time scale, the observational density in terms of space is low mainly due to the high expense of constructing tide gauge stations. In this work, we designed a novel tide monitoring technique with muography that could be operated in near-shore basements (or similar structures on land below sea level) and found that more practical, stable, robust and cost-effective high-spatiotemporal-density tide measurements are possible. Although the time resolution, sensitivity, and the distance between the detectors and the shorelines are tradeoffs, hourly and annual sensitivity (ability to detect the tide height variations) of less than 10 cm and 1 mm can be statistically attained, respectively. It is anticipated that the current muographic technique could be applied as an alternative, cost-effective and convenient dense tidal monitor network strategy in coastal areas worldwide.

Introduction

Recently flood hazards have increased, which have been exacerbated by a rising global mean sea level due to land ice melting and ocean warming[1,2,3]. One of the most important factors to quantify the extent of this increase is the flood hazard magnification rate[4]. Utilizing data from several years of tide gauge observations of various extreme weather and flooding events has been the most common way to determine this amplification[5,6,7]. Tidal levels have been measured and monitored in order to obtain reliable sea-level information including tides, surges, waves, and relative sea-level rise. Such information is essential for coastal communities since coastal flooding is increasingly occurring in many areas[8,9]. Also, understanding of the regional tide streams in the inner bay is important for the safety of navigation and environmental assessments, as well as to improve assessments of regional seawater circulation types and pollution distribution, and tidal flow fields studies, which have been numerically modeled in various regions [10,11,12,13,14]. In order to create accurate modeling for both forecasting storm surges and estimating tidal fields spatiotemporally, high density tide level information is required as a boundary condition. However, since tide gauge stations (TGSs) are expensive and usually have to be deployed in wave-sheltered harbors, these are only sparsely distributed even within large metropolitan bay areas[15]. For this reason, the tide level data have been interpolated to reproduce the continuity and smoothness of the tide level distribution[16]. Moreover, TGSs measure only Still Water Levels (SWLs) on the spot, and as a consequence, we tend to underestimate or exclude waves that include wave setup and wave run-up[17,18,19](Figure 1). These tide gauge-based estimates of the amplification of extreme water levels therefore are not always accurately assessing actual shoreline conditions outside the wave shelter.

Satellite-based radar altimetry provides a more global solution for analyzing tidal changes in wider areas. However, space-time resolutions depend on a satellite's repeat period: 10 days to 35 days depending on the satellite orbit[20]. Also, the validity of measurements close to the coast is limited and may not accurately represent the coastal processes[21]. Global-navigation-satellite-system (GNSS) buoys using GNSS satellite positioning technology may solve this problem with faster time resolutions (30 s – 1 day)[22]. However, installing buoys in the high maritime traffic areas is not practical. Moreover, the deployment and data transfer costs tend to be high. Ocean bottom sensors such as pressure and ultrasonic gauges provide tidal information in realtime[23]. However, since these sensors have to be directly located on the seafloor, preparation of infrastructures for electricity and data transfer are expensive. Moreover, pressure gauges have an intrinsic drift error, and the propagation time of the ultrasonic signals depend on solar radiation, seasonal cycles, mixing of the water due to sea currents, and the presence of rivers or waste waters[24].

Recently, muography, which has been conducted from an underwater tunnel showed the potential to offer a practical real-time tide monitor without intrinsic drift errors, and without the requirement to provide infrastructures for electricity and data transfer[15]. Due to the penetrative and ubiquitous nature of cosmic-ray muons, they have been utilized as probes for muography and have been widely applied to visualizing the internal structure of gigantic objects. Muographs (muographic observation and recording devices) have been deployed to observe targets such as volcanoes[25,26,27,28,29,30,31,32,33,34], rock overburdens[35,36,37], and cultural heritage sites[38,39,40,41] (typically being positioned below the targeted region) to record muographic images of these land objects, but as mentioned above more recently, the Hyper Kilometric Submarine Deep Detector (HKMSDD) realized the goal of underwater muography imaging at reasonable costs by installing muographs inside an underwater tunnel. However, underwater tunnels are not always available in coastal areas that would benefit the most from muography monitoring. In this work, an alternative to using underwater tunnels is proposed: HKMSDD muon sensor modules (HKMSDD-MSMs) could be deployed in coastal regions globally within available near-shore basements (or similar structures on land sufficiently below sea level), and could be applied as a convenient, dense and standalone tidal monitoring network or in tandam with another network.

Results

Principle. Galactic cosmic rays (GCRs) are accelerated by high energy events in our galaxy and before they arrive at Earth, they are deflected multiple times during their propagation, and lose their initial directional information. Muons are produced in the Earth's atmosphere via the collision between these GCRs and the Earth’s atmospheric nuclei. Due to different atmospheric thicknesses and density gradients for different GCR's arrival angles, the muon energy spectrum varies according to the different zenith angles. As a consequence, the vertical muon flux is higher than the horizontal flux, but the average energy of vertical muons is lower than the horizontal ones. The HKMSDD-MSM tide monitor utilizes these near horizontal muons.

Figure 2 shows the principle of HKMSDD-MSM tide monitoring. In this scheme, HKMSDD-MSMs are placed at near-shore locations below sea level such as basements of commercial buildings, subway stations, underground parking lots etc. As shown in Figure 2, near horizontal muons would pass through seawater and land soil before arriving at the MSM. The total thickness of the materials that muons will traverse through before arriving at the MSM is:

$L = D/\cos\theta + (d-H)/\sin\theta$ (m.w.e.) (1)

where D (m) is the distance between the MSM and the shoreline, H (m) is the land altitude measured from the lowest tide level, d (m) is the depth of the MSMs measured from ground level, and θ is the elevation angle. Here the average densities of the land soil (ρ_{earth}) and seawater (ρ_{water}) were respectively assumed to be 2.0 gcm^{-3} and 1.0 gcm^{-3}. Since the tide level variations Δh (m) only changes the second term of Eq. (1), as D increases, the MSM's sensitivity to the tide variations is degraded.

The muon flux observed at the MSM (N) can be calculated as follows. Once L is determined, the minimum muon energy (E_c) that arrives at the MSM can be derived from the muon's energy range relationship in H_2O and SiO_2[42]. By integrating the open-sky muon energy spectrum[43,44,45] over the energy range between E_c and infinity, we obtain the angular dependent integrated muon flux $I(\theta)$, where θ is elevation angle. By integrating $I(\theta)$ over the angular range between 0 and Θ, N is derived, where Θ holds the following relationship:

$\tan\Theta = (d-H)/D$ (2)

Figure 3 shows I as a function of the elevation angle ($\theta < \Theta$) for different D. As long as $\theta < \Theta$, the soil portion in L relies only on D and θ. Therefore, as the distance between the MSM and the shoreline increases, the number of muons that arrives at the MSM will decrease. As a consequence, the time resolution of the HKMSDD-MSM tide monitor will be degraded as the length of D increases.

Case studies in Tokyo Bay. Urban underground spaces (UUSs) have various functions: storage, industry, transport, utilities and communications and public use. In Tokyo, most of the underground facilities in the city areas are for public use. Tokyo uses more than 50% of UUSs for transportation including subways, highway tunnels, and stations, and almost 40% of UUSs for public spaces, shopping areas, parking lots, storages and industrial use[46]. Throughout its historical development, UUSs in Tokyo have progressed from shallow to deep soil layers. Therefore, inside UUSs, the supply of stable utility (electricity, gas and water) is one of the most important factors. In Japan, the UUSs for public use are equipped with a three-step power failure prevention system. In particular, there is a regulation that a UUS with a floor area exceeding 1,000 m^2 must be equipped with an independent emergency power generator by a UUS managing body. If the emergency power generator is shut down for some reason, it will be immediately replaced with a battery-operated system. Such a robust pre-installed infrastructure particularly designed for UUSs also offers an ideal space for stable and safe operations of muographic tide monitors even under extreme conditions such as severe storms and earthquakes.

The south-central Tokyo map in Figure 4 shows the distribution of Tokyo deep and large-scale UUSs (DLUUSs) located in the regions within 200 m from the shorelines. Here, the DLUUSs are defined as those having basement floors located below sea level with a floor size exceeding 1,000 m^2. The south-central part of Tokyo consists of the main land and more than 15 islands in the north part of Tokyo Bay. Most of these islands are connected by bridges, but lines on the ocean in Figure 4 represent railway/motor underwater tunnels which connect these islands. A number of commercial sky scrapers were built on these islands, and some of them have UUSs reaching depths greater than 10 m from the ground surface. Since the elevation of these islands ranges between 1 m and 7 m, these floors are located below sea level.

HKMSDD-MSM. Figures 5 and 6 show close and vertical cross-sectional views of some representative UUSs indicated in Figure 4. As can be seen in this figure, other islands are located along the muon trajectories. These islands may degrade the quality of tide monitoring and thus this effect will be later discussed.

Figure 7 shows the proposed HKMSDD-MSM muograph design for the tide monitoring network. HKMSDD-MSM consists of two sets of scintillation detectors that consist of plastic scintillators and photodetectors. The length and the width of the scintillators are respectively 8 m and 15 cm, making a total detection area of 1.2 m^2. There are a couple of options for photodetectors: photomultiplier tubes (PMT) or SiPM. In the former case, the PMTs are attached to the scintillators via acryl light guides. In the latter case, scintillation light is transported to SiPM via wave length shift (WLS) fibers. Since the Eljen's scintillators (EJ-208) and the Kuraray's WLS fibers (Y-11(200)) both have a long attenuation length of 4 m[47] and 3.5 m[48], respectively, one photodetector is sufficient for readout of each scintillator strip. Coincidence signals verified to be the same angle between these two detectors are recorded as muon signals. The current HKMSDD-MSM has a wide angular acceptance for the azimuthal angle (Figure 7B) and a narrow angular acceptance for the elevation angle (Figure 7C). The distance between two scintillator strips (x) is derived by dividing a double of the scintillator width (30 cm) by the observation geometry ($(d\text{-}H)/D$) (rad). In the cases shown in Figures 5 and 6, since $(d\text{-}H)/D$ is 0.125 rad (7.1°), x is 2.4 m. As shown in Figure 7A, the scintillator strips are placed so that the HKMSDD-MSM does not receive the muons arriving from the direction opposite to the sea. However, some scattered upward-going muons could generate fake tracks.

Figure 8 shows the fraction of the fake tracks generated by the scattered upward-going muons as a function of the elevation angles. The number of events were normalized to the value observed at θ = 0±16.5 mrad, where θ is elevation angle. The observation conditions to produce this plot are summarized in the Method section. Since these data were taken in the open-sky environment, it is expected that this fraction will be somewhat lower than this in an underground environment. In conclusion, with the currently proposed setup, contamination by the near horizontal backward directed muons will be suppressed to a rate below 1%, and thus this effect will be neglected in the following discussions. Figures 7B and 7C respectively show azimuthal and elevation angular acceptance of HKMSDD-MSM in the cases shown in Figures 5 and 6. As shown in Figure 7C, HKMSDD-MSM does not have an acceptance for the angular region beyond 7.1°. This design helps to avoid recording muons that didn't pass though seawater, which would eventually degrade the sensitivity to Δh.

Figures 9 and 10 show the muon flux and detectable tide level variations Δh as a function of the distance between the MSM and the shoreline (D) for different depths (5 m and 15 m) from the mean sea level. Here the detectable Δh was derived from the standard deviation of the number of muons (ΔN) recorded with the proposed detector configuration (Figure 7). For longer D, muographs located at deeper locations would record more muons per unit time; hence would produce better resolutions for determining Δh since both the angular acceptance and the average elevation angle of incoming muons decrease. As the MSM depth (d) increases, the total solid angle required to accept muons at the MSM increases, however, since the ratio $\Delta h/(d\text{-}H)$ decreases, sensitivity of the Δh detection or time resolution is degraded. These two factors are tradeoffs. The conclusion for dealing with this situation is as follows. For the purpose of real time monitoring (< 1hour), the distance between the MSM and the shoreline (D) has to be less than 50 m and 20 m to attain Δh < 50 cm and Δh < 10 cm, respectively. For the purpose monitoring with a longer time scale, if D is less than 20m, sub millimeter accuracy can be obtained per year. From this plot, we also can find that if the MSM depth is shallower, better Δh resolution is achievable for shorter D, but better Δh resolution is achievable for longer D if the MSM depth is deeper. This is because even the ground soil thickness along the muon path is thicker; hence degrading sensitivity to Δh, for longer D, the MSM's acceptance solid angle is larger if the MSM depth is deeper.

The current muographic tide monitor measures the tide height averaged over the shoreline to offshore, however, the muon's path length in seawater increases; hence the number of muons decreases as an elevation angle of incoming muons decreases and thus, the observed tide levels are representing those in the near-shore regions. Figure 11 shows the fraction of the number of muons out of the total number of muons (integrated over the entire angular region) as a function of the distance from the shore line for different distances between the MSM and the shoreline (D). As can be seen in this figure, the effect of the islands located further than 200 m from the MSM is negligible. In Cases (A) and (B) (Figures 5 and 6), since the depth of the MSM is 5 m from sea level, more than 95% of muons pass through the seawater located between the islands.

Discussion

In urban areas, space on the ground is usually already occupied by buildings and structures, with typically only underground space to utilize as locations for new facilities. Although extra costs are required for ventilation and emergency prevention and response systems, no maintenance of outer walls is needed and, in many cases, underground facilities require less temperature adjustment in comparison to above ground spaces. Moreover, deep underground structures suffer significantly less damage from earthquakes than structures above. Consequently, cities with high population densities tend to develop more UUSs.

The currently proposed muographic tide monitor is based on the successful, stable and maintenance free long-term observation of the Tokyo-bay Seafloor HKMSDD (TS-HKMSDD) at a DLUUS (highway tunnel) in Tokyo. As shown in Figure 12, since we started the TS-HKMSDD stable operation mode in April, 2021, TS-HKMSDD has successfully recorded the tide level variations without interruption, and will continue to record the tide level variations without any intermittency or measurement drift. On the other hand, TGS observations frequently give erroneous data[49]. During the measurements, data can be suddenly corrupted with noise, or (due to mechanical problems) the moving parts of the gauge may lock up or malfunction[49]. Unlike tide gauges or buoys, since HKMSDD doesn't have to be exposed to harsh environments, and there aren't any mechanically moving parts in HKMSDD. This would also be the case for the proposed HKMSDD-MSMs setup; additionally, since DLUUSs such as commercial buildings or highway tunnels have a robust electric and internet environment with a private power generation backup system, it is anticipated that muographic tide monitors will function more stably than any other legacy tide level monitors.

The costs required for producing a muographic tide monitor will be less than 6,000 US dollars (USD) (3,000 USD for a 1-m^2 plastic scintillator sheet, 2,000 USD for a 2 PMTs, and 500 USD for a readout electronics unit), which is much lower than the costs (200,000 USD[50]) required for constructing tide gauge stations. More than 30 nodes of a muographic tide monitor network would be possible within this budget. Moreover, a currently developing stainless welded proportional counter (SWPC) will further reduce the costs for deployment. Since the SWPC structure is simple (consisting of a tungsten wire and a stainless steel tube), the price of one node of the tide monitor network could be reduced to less than 1,000 USD in the future. This simple structure also makes it environmentally robust. The HKMSDD-MSM technique is directly applicable to any coastal cities in the world, such as New York, Boston, Miami, San Francisco, Hawaii, Tokyo, Amsterdam, Lisbon, Valencia, Venice, Naples, Marseille, Copen Hagen, etc. and it is expected that as cities continue to be more populated, potential muograph locations will also increase.

The currently proposed technique is applicable not only to near-shore DLUUSs, but also to the land lying below sea level such as many regions of the Netherlands. In such countries, spatiotemporally dense tidal measurements are particularly important for accurate forecasting of storm surges. In the Netherlands, a warning system has been developed and operated by the Dutch storm surge warning service (SVSD) in cooperation with the Royal Netherlands Meteorological Institute (KNMI). The system is based on a numerical hydrodynamic model called the Dutch continental shelf model (DCSM)[49]. Since the 1990s, the accuracy of the system has been improved by incorporating observations of tide gauges. KNMI's automatic production line (APL) has been developed to produce numerical forecasts. However, during the course of this automatic production, the assimilation of only a small number of erroneous observation data will harm the forecast. Figure 13 shows an example of locations in Wadden Sea that would be appropriate for installation of HKMSDD-MSMs. The areas marked along the shore lines are significantly lower than sea level (< -2 m) and thus, the proposed muographic monitors could be simply placed on the ground floor in any building near shore lines to start tide measurements. By incorporating a low-cost, dense, robust muographic tide monitor network to work in conjunction with the existing system, the quality and accuracy of forecasts would be improved.

Quality of the tidal observations depend on observational density in space and time. With current tidal measurements, high observational density in time is possible but spacial observational density is low.. In order to address sub-hourly processes such as meteotsunamis to seasonal and interannual tidal variations, short special scales associated with the high frequency variables have to be covered[21]. The continuity and the smoothness of the spatiotemporal series of total water level, surge and the deviation would be desired and this is achievable with HKMSDD-MSM.

Method

Scattered upward-going muon measurements. Figure 14 shows the experimental setup for measuring scattered upward-going muons. The experimental setup consists of 6 MSM layers and 5 lead blocks for radiation shielding. Thickness of each lead block is 100 mm. Each MSM layers consist of 15 horizontally and 15 vertically aligned MSMs. Each MSM measures 1,500 mm in length, 100 mm in width, and 20 mm in thickness. The distance between the uppermost-stream detector and the lowermost-stream detector was 3,000 mm. Therefore, the azimuthal (Φ) and elevation (Θ) viewing angle are respectively ±460 mrad (±26^{o}) and 460 mrad (26^{o}), the angular resolution was 33 mrad, and only linear trajectories were recorded as muon events. There is a mountain right in front of one side of this setup, but there are no obstacles on the other side of this setup. Here, we define the open-sky direction as the forward direction and the mountain side direction as the backward direction. The rock thicknesses have a tendency to gradually decrease from the direction (1) to the direction (3) in Figure 14, but they are thicker than 2,000 m for the muons arriving the detector at elevation angles less than 100 mrad. Since the flux of the 100-mrad muons after passing through 2,000-m rock is $4.2\text{x}10^{-4}$ $m^{-2}sr^{-1}s^{-1}$, which is equivalent to 1/2,500 of the open-sky flux of muons arriving at the same elevation angle, the muonic component that directly arrived from the backward direction out of the entire events recorded as backward-directed muons were assumed to be zero for elevation angles less than 100 mrad in this experiment. The plot shown in Figure 8 was obtained by integrating the number of muons (N) over the azimuthal angle range between -Φ and Φ for different elevation angles (θ). The geometrical acceptance of the current setup was applied to correct the elevation-angle distribution.

Declarations

Contributions

H.K.M.T. wrote the text. H.K.M.T. prepared the figures. H.K.M.T. reviewed the manuscript.

Corresponding author

Correspondence to Hiroyuki K. M. Tanaka.

Ethics declarations

Competing interests

The authors declare no competing interests.

References

1. Hunter, J. A simple technique for estimating an allowance for uncertain sea-level rise. Clim. Change. **113**, 239–52 (2012).
2. Tebaldi, C., Strauss, B. H., Zervas, C. E. Modelling sea level rise impacts on storm surges along us coasts. Environ. Res. Lett. **7**, 014032 (2012).
3. Gregory, J. M. *et al.* Concepts and terminology for sea level: Mean, variability and change, both local and global. Surv. Geophys. **40**, 1251–89 (2019).
4. Haasnoot, M., Kwakkel, J. H., Walker, W. E., TerMaat, J. Dynamic adaptive policy pathways: A method for crafting robust decisions for a deeply uncertain world. Glob. Environ. Change **23**, 485–98 (2013).
5. Slangen, A. *et al.* The impact of uncertainties in ice sheet dynamics on sea-level allowances at tide gauge locations. J. Mar. Sci. Eng. **5**, 21 (2017).
6. Rasmussen D. J. *et al.* Extreme sea level implications of 1.5°C, 2.0°C and 2.5°C temperature stabilization targets in the 21st and 22nd centuries. Environ. Res. Lett. **13**, 034040 (2018).
7. Frederikse T. *et al.* Antarctic ice sheet and emission scenario controls on 21st-century extreme sea-level changes. Nat. Commun. **11**, 390 (2020).
8. Nicholls, R. J. *et al.* Sea-level rise and its possible impacts given a 'beyond 4°C world' in the twenty-first century. Philos. Trans. R. Soc. A **369**, 161–181 (2011).
9. Dahl, K. A., Fitzpatrick, M. F. & Spanger-Siegfried, E. Sea level rise drives increased tidal flooding frequency at tide gauges along the US East and Gulf Coasts: Projections for 2030 and 2045. PLoS One **12**, e0170949 (2017).
10. Guo, X. & Yanagi, T. Three-dimensional structure of tidal current in the East China Sea and the Yellow Sea. J. Oceanogr. **54**, 651–668 (1998).
11. Ji, Z. G. *et al.* Three-dimensionalmodeling of hydrodynamic processes in the St. Lucie Estuary. Estuar. Coast. Shelf Sci. **73**, 188–200 (2007).
12. Stanev, E. V. Understanding Black Sea dynamics: Overview of recent numerical modelling. Oceanography **18**, 56–75 (2005).
13. Lermusiaux, P. F. J. Evolving the subspace of the three-dimensional multiscale ocean variability: Massachusetts Bay. J. Mar. Syst. **29**, 385–422 (2001).
14. Gao, X. & Yanagi, T. Three dimensional structure of tidal currents in Tokyo Bay, Japan. Lamer **32**, 173–185 (1994).

15. Tanaka, H.K.M., Aichi, M., Bozza, C. *et al*. First results of undersea muography with the Tokyo-Bay Seafloor Hyper-Kilometric Submarine Deep Detector. Sci Rep **11**, 19485 (2021). https://doi.org/10.1038/s41598-021-98559-8
16. Matsumoto, K. *et al.* GOTIC2: A program for computation of oceanic tidal loading effect. J. Geod. Soc. Jpn. **47**, 243–248 (2001).
17. Melet, A. *et al.* Under-estimated wave contribution to coastal sea-level rise. Nat. Clim. Change. **8**, 234–9 (2018).
18. Woodworth, P. L. *et al.* Forcing factors affecting sea level changes at the coast. Surv. Geophys. **40**, 1351–97 (2019).
19. Dodet, G. *et al.* Wave runup over steep rocky cliffs. J. Geophy. Res. **123**, 7185–205 (2018).
20. Coles, S. An Introduction to Statistical Modeling of Extreme Values (Springer, 2001).
21. Frank Comas, A *et al.* Implementation of a low-cost ultra-dense tide gauge network in the Balearic islands (2021). Retrieved from https://upcommons.upc.edu/handle/2117/356134.
22. Liu, N. *et al.* High spatio-temporal resolution deformation time series with the fusion of InSAR and GNSS data using spatio-temporal random effect model. IEEE Trans. Geosci. Remote Sens. **57**, 1–17. https://doi.org/10.1109/TGRS.2018.2854736 (2018).
23. Testut, L. The sea level at Port-aux-Français, Kerguelen Island, from 1949 to the present. Ocean. Dyn. **56**, 464–472 (2006).
24. Lourey, M. J., Dunn, J. R. & Waring, J. A mixed-layer nutrient climatology of Leeuwin Current and Western Australian shelf waters: Seasonal nutrient dynamics and biomass. J. Mar. Syst. **59**, 25–51 (2006).
25. Jourde, K. et al. Muon dynamic radiography of density changes induced by hydrothermal activity at the La Soufrière of Guadeloupe volcano. Sci. Rep. **6**, 33406 (2016).
26. Rosas-Carbajal, M. et al. Three-dimensional density structure of la soufriére de Guadeloupe lava dome from simultaneous muon radiographies and gravity data. Geophys. Res. Lett. **44**, 6743–6751 (2017).
27. Tanaka, H. K. M. et al. High resolution imaging in the inhomogeneous crust with cosmic-ray muon radiography: The density structure below the volcanic crater floor of Mt. Asama, Japan. Earth Planet. Sci. Lett. **263**, 104113 (2007).
28. Tanaka, H. K. M. *et al.* Imaging the conduit size of the dome with cosmic-ray muons: The structure beneath Showa-Shinzan Lava Dome, Japan. Geophys. Res. Lett. **34**, 053007 (2007).
29. Tanaka, H. K. M., Uchida, T., Tanaka, M., Shinohara, H. & Taira, H. Cosmic-ray muon imaging of magma in a conduit: Degassing process of Satsuma-Iwojima Volcano, Japan. Geophys. Res. Lett. **36**, L01304 (2009).
30. Tanaka, H. K. M., Kusagaya, T. & Shinohara, H. Radiographic visualization of magma dynamics in an erupting volcano. Nat. Commun. **5**, 3381 (2014).

31. Tanaka, H. K. M. Instant snapshot of the internal structure of Unzen lava dome, Japan with airborne muography. Sci. Rep. **6**, 39741 (2016).
32. Olah, L., Tanaka, H. K. M., Ohminato, T. & Varga, D. High-definition and low-noise muography of the Sakurajima volcano with gaseous tracking detectors. Sci. Rep. **8**, 3207 (2018).
33. Lo Presti, D. et al. Muographic monitoring of the volcano-tectonic evolution of Mount Etna. Sci. Rep. **10**, 11351. https://doi.org/10.1038/s41598-020-68435-y (2020).
34. Tioukov, V. et al. First muography of Stromboli volcano. Sci. Rep. **9**, 6695 (2019).
35. Tanaka, H. K. M. Muographic mapping of the subsurface density structures in Miura, Boso and Izu peninsulas, Japan. Sci. Rep. **5**, 8305 (2015).
36. Thompson, L. F. et al. Muon tomography for railway tunnel imaging. Phys. Rev. Res. **2**, 023017. https://doi.org/10.1103/PhysRevResearch.2.023017 (2020).
37. Oláh, L. et al. CCC-based muon telescope for examination of natural caves. Geosci. Instrum. Method Data Syst. **1**, 229–234 (2012).
38. Cimmino, L. et al. 3D muography for the search of hidden cavities. Sci. Rep. **9**, 2974. https://doi.org/10.1038/s41598-019-39682-5 (2019).
39. Saracino, G. et al. Imaging of underground cavities with cosmic-ray muons from observations at Mt. Echia (Naples). Sci. Rep. **7**, 1181 (2017).
40. Tanaka, H. K. M., Sumiya, K. & Oláh, L. Muography as a new tool to study the historic earthquakes recorded in ancient burial mounds. Geosci. Instrum. Method Data Syst. **9**, 357–364. https://doi.org/10.5194/gi-9-357-2020 (2020).
41. Morishima, K. et al. Discovery of a big void in Khufu's Pyramid by observation of cosmic-ray muons. Nature **552**, 386–390 (2017).
42. Groom, D. E. *et al.* Muon stopping-power and range tables: 10 MeV–100 TeV. At. Data Nucl. Data Tables **78**, 183–356 (2001).
43. Allkofer, O.C. *et al.* Cosmic ray muon spectra at sea-level up to 10 TeV. Nucl. Phys. B **259**, 1–18 (1985).
44. Jokisch, H. *et al.* Cosmic-ray muon spectrum up to 1 TeV at 75° zenith angle. Phys. Rev. D **19**, 1368 (1979).
45. Achard, P. *et al.* Measurement of the atmospheric muon spectrum from 20 to 3000 GeV. Phys. Lett. B **598**, 15–32 (2004).
46. Bobylev, N. Mainstreaming sustainable development into a city's Master plan: A case of Urban Underground Space use. Land Use Policy **26**,1128–1137 (2009).
47. Eljen Technology. General purpose of EJ-200, EJ-204, EJ-208, EJ-212. (2022). Retrieved from https://eljentechnology.com/products/plastic-scintillators/ej-200-ej-204-ej-208-ej-212).
48. Kuraray. Wavelength Shifting Fibers. (2022). Retrieved from http://kuraraypsf.jp/psf/ws.html)
49. Verlaan, M. *et al.* Operational storm surge forecasting in the Netherlands: Developments in the last decade. Philos. Trans. Royal Soc. A **363**, 1441–1253 (2005).

50. The Ministry of Land, Infrastructure, Transport and Tourism, 2011 administrational enterprise review sheet. (2011). Retrieved from https://www.mlit.go.jp/common/000169227.pdf

Figures

Figure 1

Conceptual view of muography for tide monitoring. The label TGS stands for a tide gauge station, and Mu indicates the location of a muograph (muographic observation and recording device). Green arrows indicate muon trajectories. HKMT drew this image with Microsoft PowerPoint software and holds the copyright.

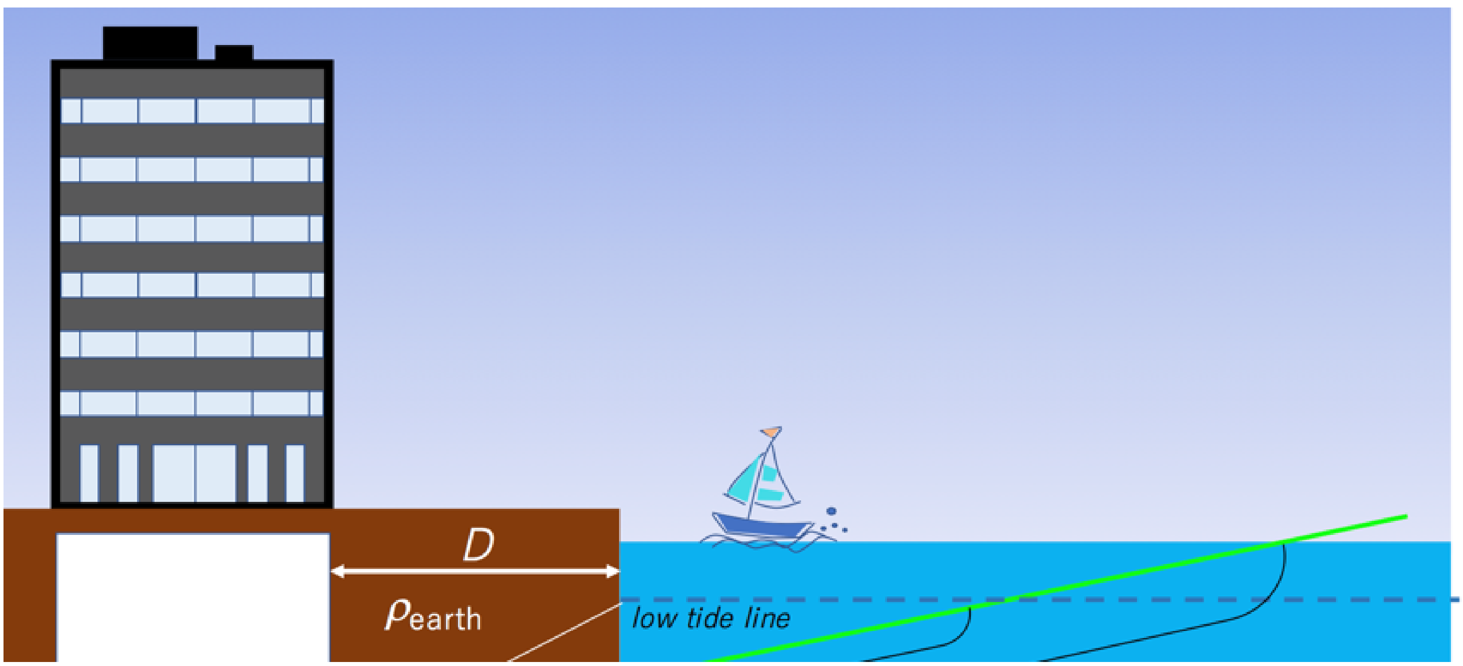

Figure 2

Principle of HKMSDD-MSM tide monitoring. The green arrow and the label Mu indicate respectively the muon trajectory and the location of the HKMSDD-MSM. HKMT drew this image with Microsoft PowerPoint software and holds the copyright.

Figure 3

Integrated muon flux as a function of the elevation angle for different distances: 0 m (blue), 25 m (red), 50 m (gray), 100 m (yellow), and 150 m (light blue) between the MSM and the shoreline.

Figure 4

South-central Tokyo map showing the distribution of the Tokyo deep and large-scale urban underground spaces (UUSs) located in the regions within 200 m from the shorelines. Commercial UUSs including subway stations, shopping areas and parking lots (filled red circles) and underwater tunnels (red bold lines) are shown. Dashed lines indicate the ocean lines. HKMT drew this map with Microsoft PowerPoint software and holds the copyright.

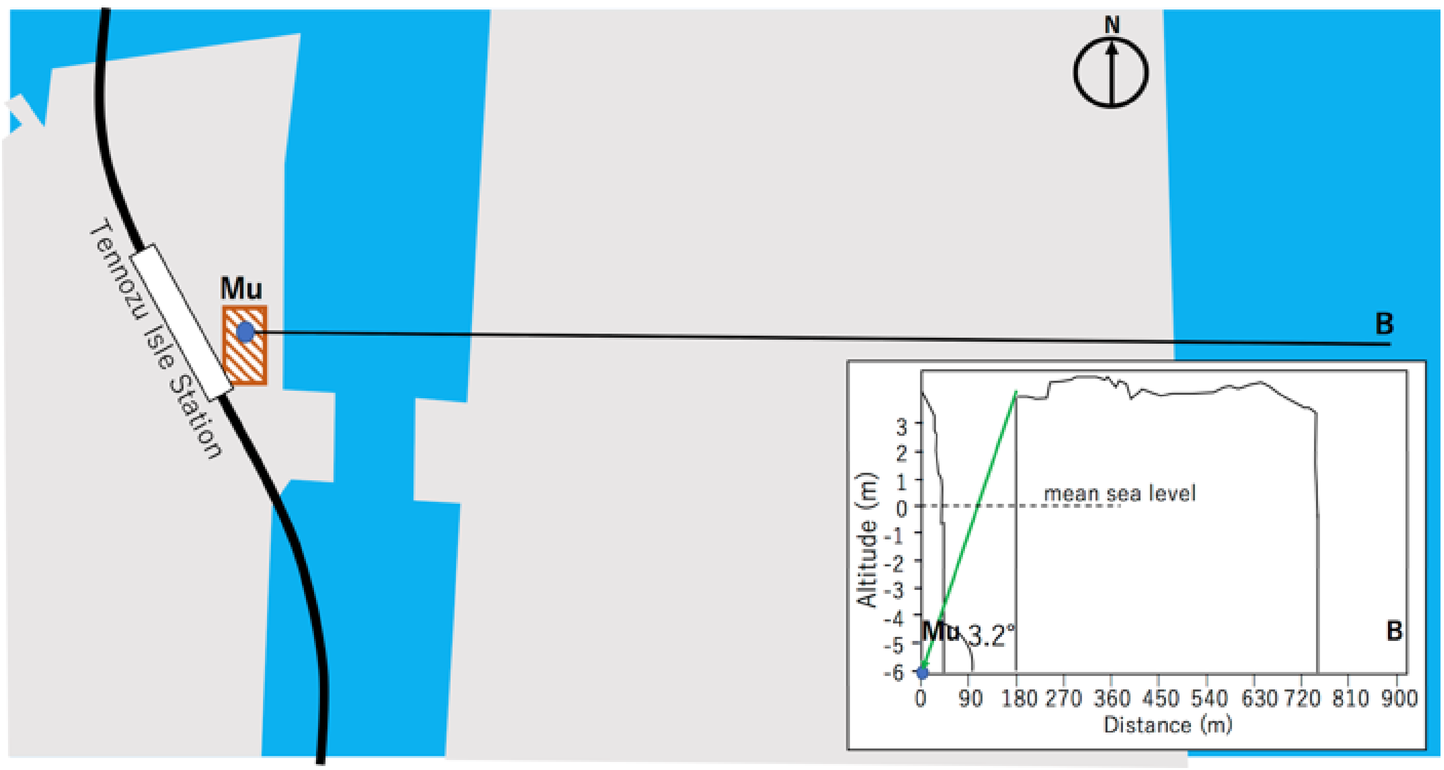

Figure 5

Enlarged map near the region of (1) in Figure 4. The red shaded rectangle indicates a commercial building having a basement floor located 10 m below the ground surface. The label Mu indicates the location of the HKMSDD-MSM. The inset shows the cross-sectional view along the Mu-B line. The elevation scale is magnified by 50 times of the horizontal scale. HKMT drew this map with Microsoft PowerPoint software and holds the copyright.

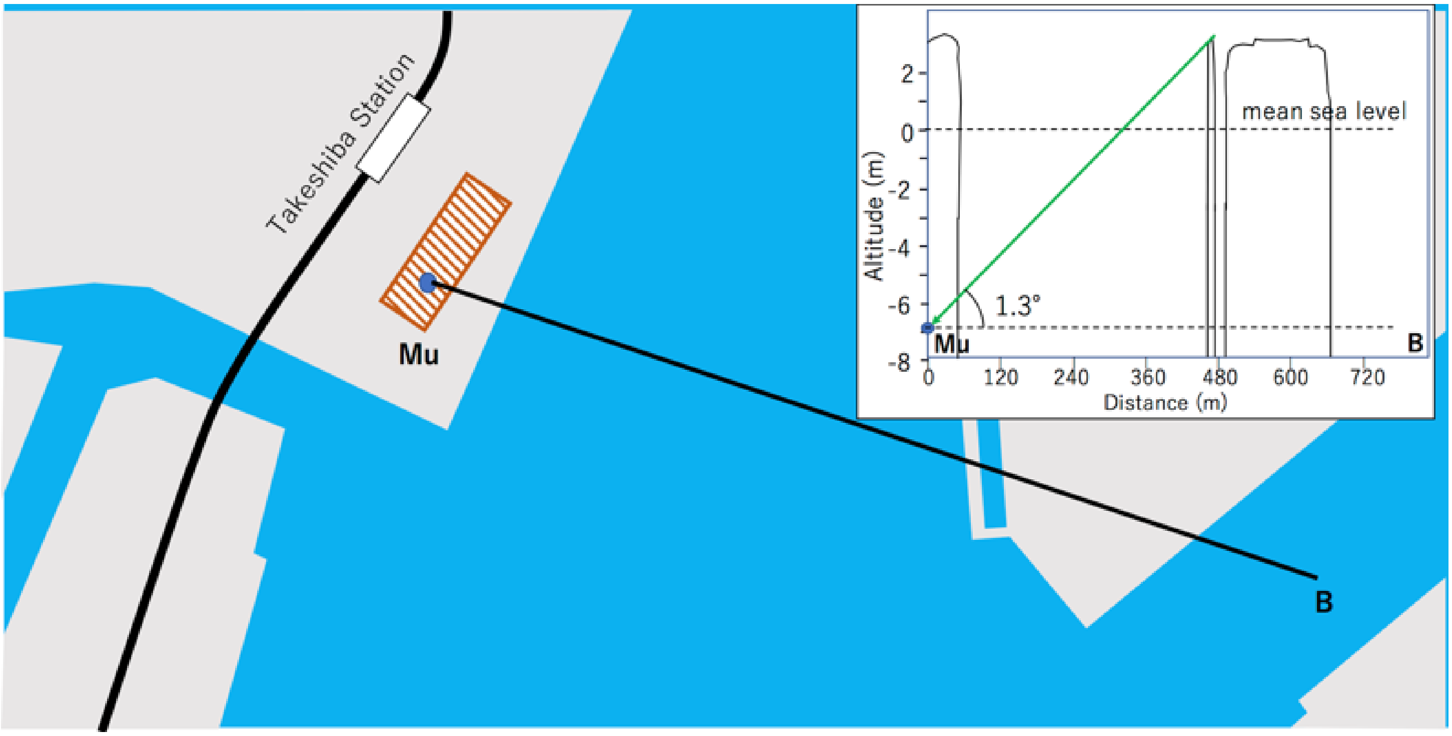

Figure 6

Enlarged map near the region of (2) in Figure 4. The red shaded rectangle indicates a commercial building having a basement floor located 10 m below the ground surface. The label Mu indicates the location of the HKMSDD-MSM. The inset shows the cross-sectional view along the Mu-B line. The elevation scale is magnified by 50 times of the horizontal scale. HKMT drew this map with Microsoft PowerPoint software and holds the copyright.

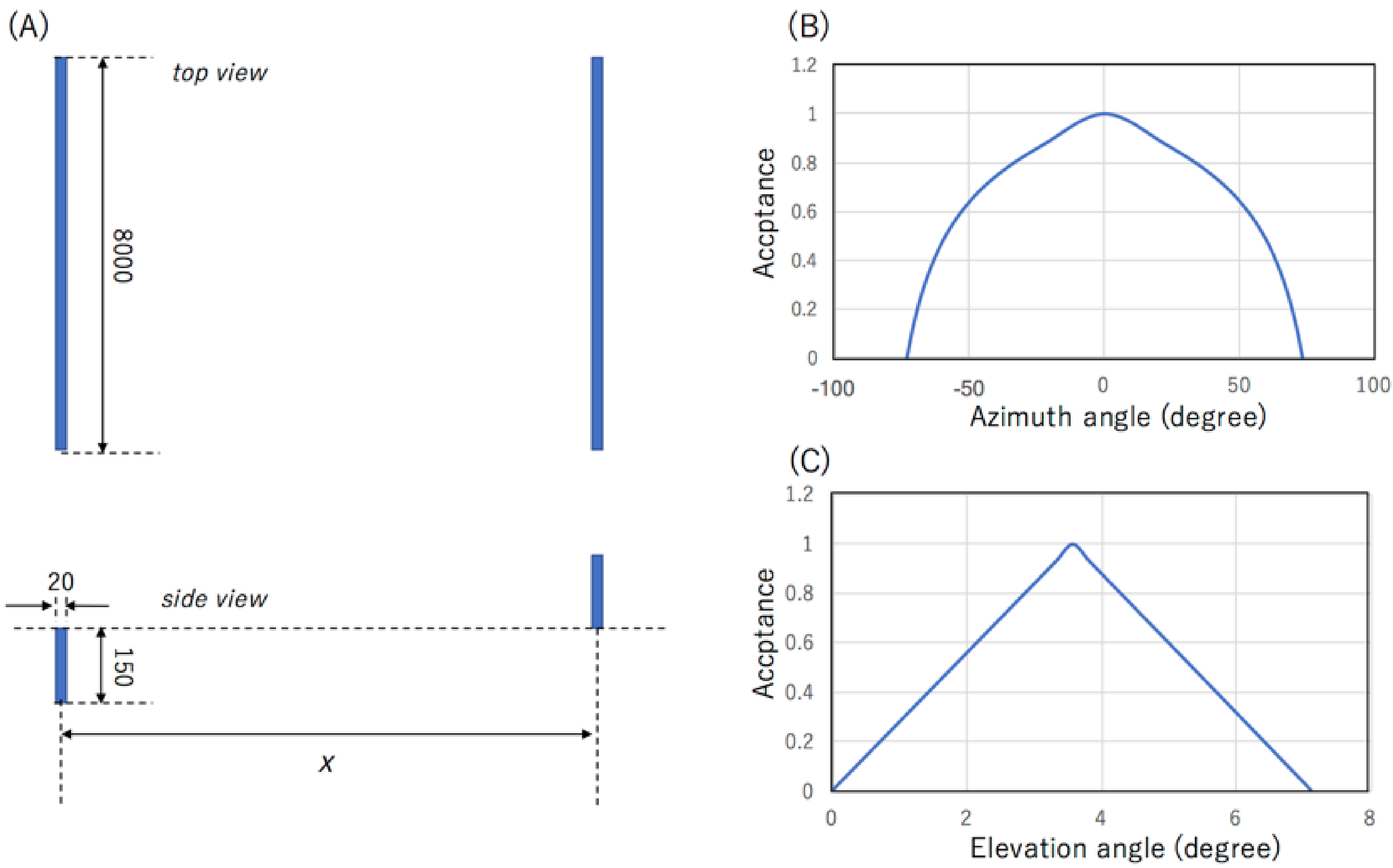

Figure 7

Geometric configuration of HKMSDD-MSM for the tide monitoring network. The top and side views of the setup are respectively shown in the top and bottom panel of (A) in units of mm. The azimuthal (B) and elevation angle (C) acceptances for *x* =240 mm are also shown.

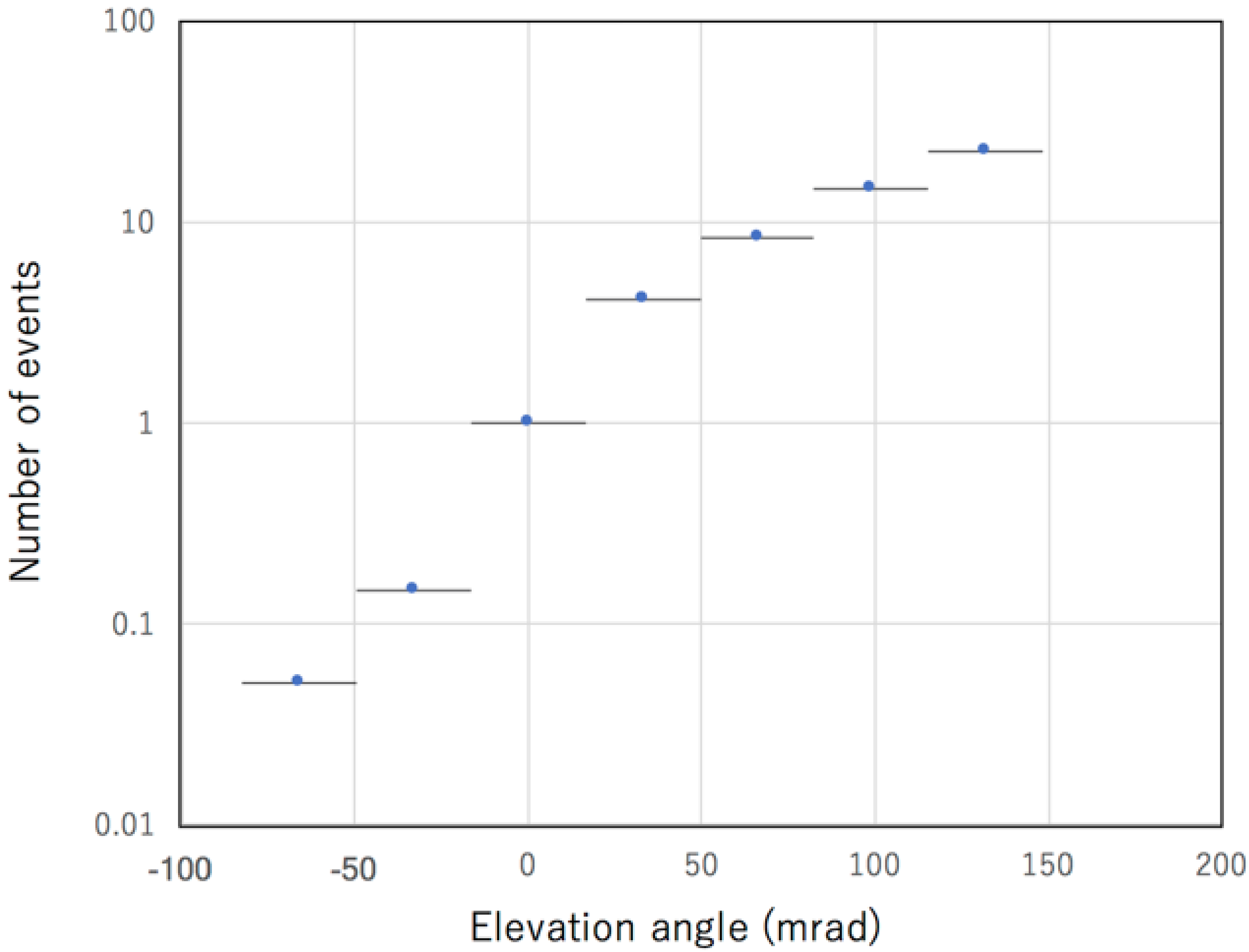

Figure 8

Fraction of the fake tracks generated by the scattered upward going muons as a function of elevation angle. Horizontal bars associated with data points indicate the angular region that occupies 75% of the total acceptance.

Figure 9

Muon flux (A) and detectable tide level variations D*h* (B and C) as a function of the distance between the MSM and the shoreline (*D*) for (*d*-*H*) = 5 m. D*h* variations are shown for different time resolutions: 10 minutes (B), 1 hour (C), and 1 year (D).

Figure 10

Muon flux (A) and detectable tide level variations D*h* (B and C) as a function of the distance between the MSM and the shoreline (*D*) for (*d*-*H*) = 15 m. D*h* variations are shown for different time resolutions: 10 minutes (B), 1 hour (C), and 1 year (D).

Figure 11

Fraction of the number of muons out of the total number of muons as a function of the distance from the shore line for different distances between the MSM and the shoreline (*D*): 25 m (red line), 50 m (gray line), 100 m (yellow line), and 150 m (blue line).

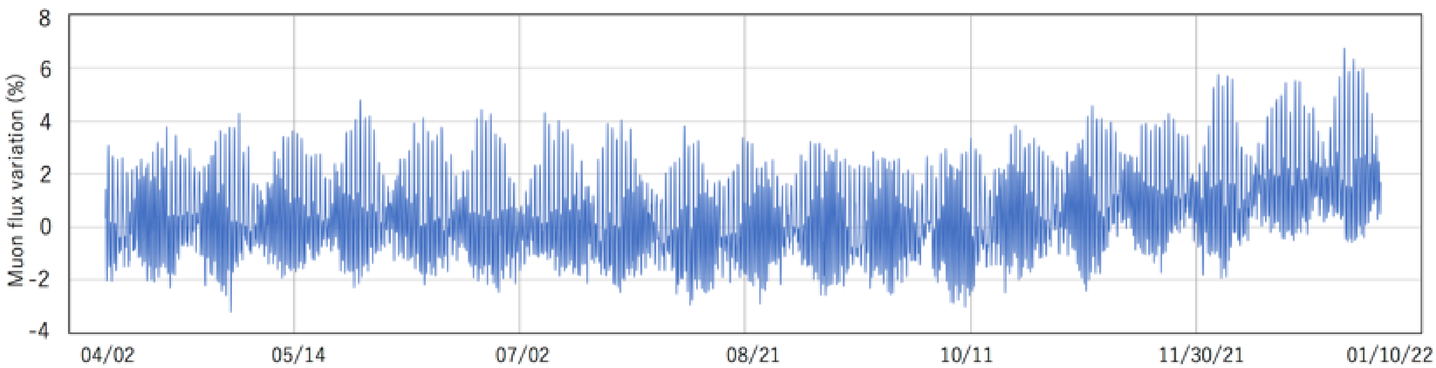

Figure 12

Tide variations recorded at TS-HKMSDD without any intermittency or measurement drift.

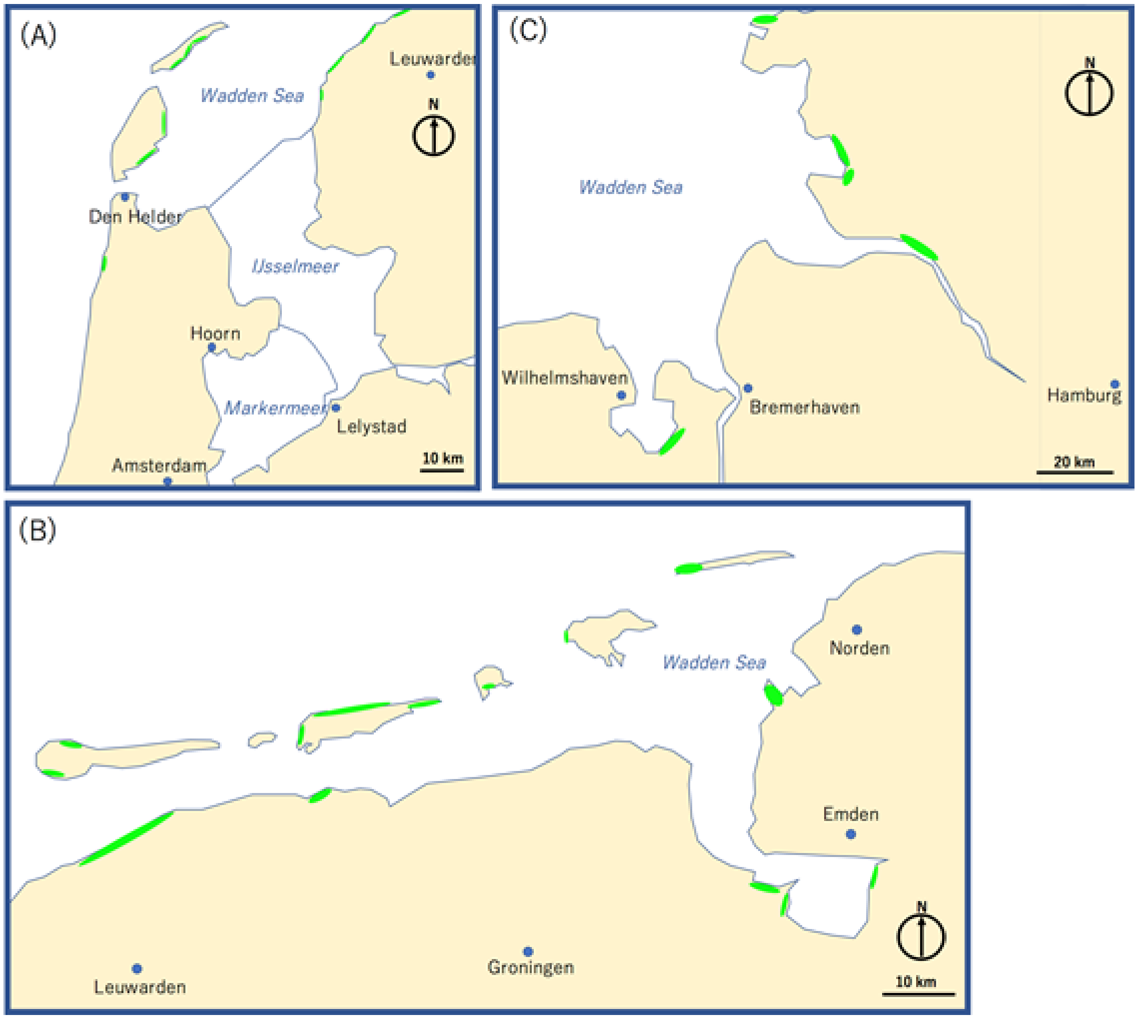

Figure 13

Possible locations of HKMSDD-MSMs in Wadden Sea. The region near Amsterdam (A), near the Netherlands-Germany border (B), and in the northwest part of Germany (C) are shown. The green areas indicate regions that are sufficiently lower than sea level (< -2 m) along the shore lines, which would be appropriate for the proposed HKMSDD-MSM technique. HKMT drew this map with Microsoft PowerPoint software and holds the copyright.

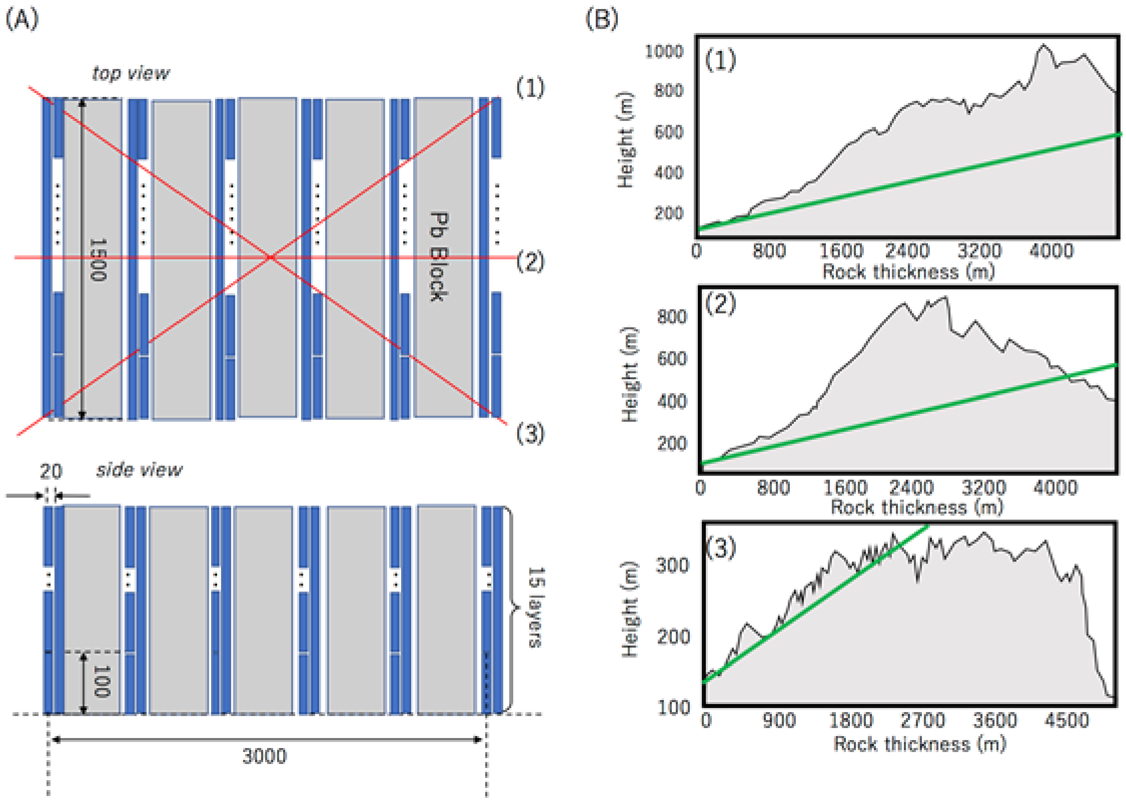

Figure 14

Experimental setup for measuring scattered upward going muons. The top and side views of the geometrical configuration of the setup is shown in (A). The units are in mm. The blue rectangles and gray rectangles respectively indicate MSMs and lead blocks. Red lines indicate the azimuthal viewing angle of the setup. The cross-sectional views of the mountain located in the backward direction are shown in (B) for both edges (1 and 3) and the center (2) of the viewing angle. Green lines indicate the trajectories of muons arriving at a 100-mrad elevation angle.